29 June 2001

ELSEVIER

Chemical Physics Letters 341 (2001) 608–618

CHEMICAL PHYSICS LETTERS

www.elsevier.nl/locate/cplett

Collision energy effects on the dynamics of the reaction $O(^3P) + CH_4(X^1A_1) \rightarrow OH(X^2\Pi) + CH_3(X^2A_2'')$

R. Sayós [a,1], Jordi Hernando [a], María P. Puyuelo [b], Pedro A. Enríquez [b], Miguel González [a,*]

[a] *Departament de Química Física i Centre de Recerca en Química Teòrica, Universitat de Barcelona, C/Martí i Franquès, 1, 08028 Barcelona, Spain*

[b] *Departamento de Química, Universidad de La Rioja, C/Madre de Dios, 51, 26004 Logroño, Spain*

Received 27 February 2001; in final form 24 April 2001

Abstract

A study of the collision energy effects on the dynamics of the title reaction was performed using the quasi-classical trajectories (QCT) method and an analytical triatomic potential energy surface recently derived by our group. Scalar and two-vector properties of the reaction were analysed in terms of the collision energy. The results obtained can be rationalised in terms of the coexistence of reactive trajectories with rebound and non-rebound features, both corresponding to an abstraction reaction mechanism. Future work should account for both the full dimensionality of the system and the possibility of quantum effects.

1. Introduction

The reaction of methane with ground-state atomic oxygen, $O(^3P)$, [1]

$$O(^3P) + CH_4(X^1A_1) \rightarrow OH(X^2\Pi) + CH_3(X^2A_2'') \quad \Delta H^0_{298\ K} = 2.480 \text{ kcal mol}^{-1} \qquad (1)$$

is a primary step in the combustion process of this hydrocarbon [2]. Its relative simplicity compared to the reactions with larger hydrocarbons allows a strong interplay between theory and experiment, thus providing a deep insight into its dynamical behaviour [3].

The kinetics of reaction (1) has been extensively studied from an experimental point of view [4–8], but only two experimental works focused on the dynamics can be found in the literature. In one of them the v_2 out-of-plane bending ('umbrella' mode) vibrational distribution of CH_3 was reported [9]. In the other one, the detection of the nascent $OH(v' = 0)$ product was performed, determining the spin–orbit, Λ-doublet and rotational distributions [10].

Reaction (1) has also been studied theoretically. Ab initio calculations at different levels have been reported for the $O(^3P) + CH_4$ system [3,11–15], showing that reaction (1) has a near-collinear $O \cdots H \cdots CH_3$ transition state. It is well established that the classical barrier height for the

* Corresponding author. Fax: +34-93-4021231.

E-mail addresses: r.sayos@qf.ub.es (R. Sayós), miguel@qf.ub.es (M. González).

[1] Also corresponding author.

0009-2614/01/$ - see front matter
PII: S0009-2614(01)00518-8

ground surface is around 13–14 kcal mol^{-1} [3,13–15] and that the transition state structure and energy for the first excited PES, which also correlates reactants with the $OH + CH_3$ asymptote, are almost identical to the ones for the lowest 1^3A PES [3,12,14]. Using ab initio data, a triatomic analytical surface (GHMS PES) treating the CH_3 group as a pseudoatom [3] and a hexa-atomic analytical surface [14] have been fitted to represent the ground 1^3A PES. An improved version of the hexa-atomic analytical PES has been reported recently [16].

From both the ab initio results and the triatomic and hexa-atomic analytical PESs derived, theoretical calculations of the rate constant have been performed for reaction (1) using different levels of the transition state theory [3,11,12,14,16]. The experimental $OH(v' = 0)$ rotational distribution was well reproduced from the results of a quasi-classical trajectories (QCT) study on the GHMS PES [3]. Also, the very small QCT $OH(v' = 1)$ population obtained [3] is consistent with the experiment. Reduced dimensionality quantum scattering calculations [17–20] have also been reported on the dynamics of reaction (1) using the hexa-atomic analytical PESs derived [14,16]. The effect of exciting the umbrella and rocking vibrations of the CH_4 molecule on the reactivity was investigated, and a close comparison between the experimental and theoretical vibrational distributions of the umbrella mode of CH_3 was presented [19]. Finally, electronically nonadiabatic coupling models have been considered to explain the experimental OH spin–orbit propensities [21].

Here, we have carried out a thorough dynamics study of reaction (1) using the QCT method and the GHMS PES [3]. Scalar and two-vector properties have been analysed in terms of the collision energy (E_T), and also a product state-resolved study of the reaction dynamics has been carried out. Finally, the microscopic reaction mechanism has been investigated. We have studied in detail not only the dynamics behaviour of reaction (1) at the experimental conditions reported, which had been already partially considered in a recent contribution [3], but also under conditions of interest still not explored in the experiments.

2. Computational method

As already mentioned, the QCT method [22–24] as implemented in the TRIQCT programme [25] was used to study reaction (1), employing the GHMS PES [3]. This triatomic analytical surface (many-body expansion) was fitted by using ab initio data for the ground PES (1^3A) through which reaction (1) evolves, and treating the CH_3 group as a pseudoatom of 15 amu located in its center of mass [3]. The PES thus obtained connects the $O(^3P) + CH_4$ asymptote with the $OH + CH_3$ products through an $O\cdots H\cdots(CH_3)$ collinear transition state that presents a classical barrier height of 13.1 kcal mol^{-1} above reactants [3]. Despite reducing the dimensionality of the system and as indicated above, the experimental $OH(v' = 0)$ rotational distribution was well reproduced using the QCT method and the GHMS PES, and the very small amount of $OH(v' = 1)$ found in the calculations was consistent with the measurements [3]. This result suggests that the methyl group motions are not strongly coupled to the motions leading to reaction at the collision energies considered. Hence, it is expected that concerning the properties of the OH product, the dynamics of reaction (1) can be quite satisfactorily reproduced with this triatomic model. This kind of modelling has also been quite successfully applied in our group to the study of the $O(^1D) + N(NO)$ [26], $O(^1D) + H(CH_3)$ [27–29] and $O(^1D) + H(OH)$ [30] reactions.

On applying the QCT method, the accuracy of the numerical integration of Hamilton's differential equations was verified by checking the conservation of total energy and total angular momentum for every trajectory, and performing back-integrations on some batches of trajectories. An integration step of 0.5×10^{-16} s and an initial distance of 10 Å between the $O(^3P)$ and the H–(CH_3) center of mass were selected. This separation ensures that the interaction energy can be neglected with respect to the available energy of reactants. The rovibrational levels of the $OH(X^2\Pi)$ product were assigned using the vibrational action variable method. Since the QCT method does not account for the $OH(X^2\Pi)$ orbital ($\Lambda = 1$) and spin ($S = 1/2$) electronic angular

momenta, as in previous works [26–30] we identified the total angular momentum quantum number excluding electronic and nuclear spins, N', of the OH molecule with the value of the rotational angular momentum quantum number derived from the QCT calculations, j', plus one.

Trajectories were run at collision energies in the interval 0.50–2.0 eV, which extend from energies close to the classical reaction threshold to considerably high values of E_T. The number of trajectories run at each collisional energy was such as to ensure a statistical error of 2% or smaller in the total reaction cross-sections. Larger number of trajectories (250 000–750 000) were run at specific collisional energies (0.65, 1.0 and 1.5 eV), for which a state-specific study of the dynamical properties was performed. For each collision energy, the rovibrational energy levels of the H–(CH_3) pseudodiatomic-molecule were sampled according to a 298 K Maxwell–Boltzmann distribution.

3. Global reaction dynamics

3.1. Scalar properties

Fig. 1a shows the total reaction cross-section, σ_r, as a function of E_T. The calculation of the values of σ_r for reaction (1) from the values of the cross-section obtained in the QCT calculations on the GHMS PES (σ_r^{GHMS}) was performed as fol-

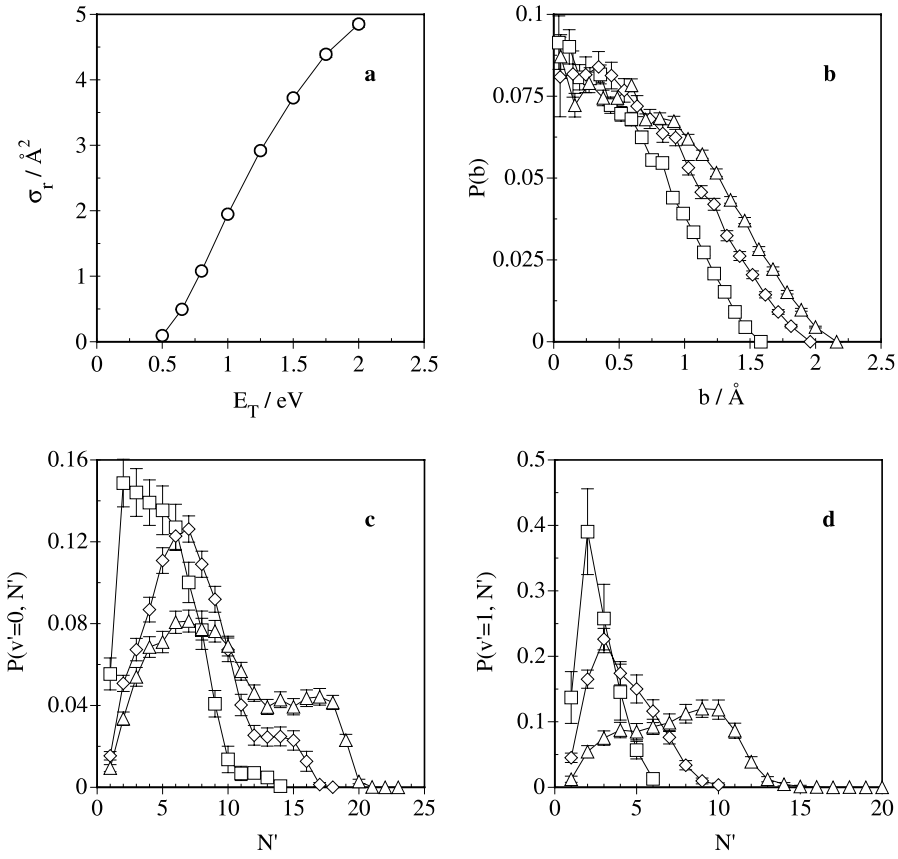

Fig. 1. (a) Global excitation function for reaction (1). (b) Opacity functions for $E_T = 0.65$ (□), 1.0 (◇) and 1.5 (△) eV. OH product rotational distributions for $v' = 0$ (c) and $v' = 1$ (d) at $E_T = 0.65$ (□), 1.0 (◇) and 1.5 (△) eV. All opacity functions and rotational distributions are normalised to unity.

lows: first, the values of σ_r^{GHMS} were multiplied by four to take into account that there are four equivalent hydrogen atoms in the methane molecule, which were assumed to react independently; second, the calculated cross-sections were multiplied by a factor of 2/3 to account for the fact that there are three adiabatic PESs correlating with the reactants asymptote ($(1)^3A' + (2)^3A''$ in C_s symmetry), but only two correlating with the $OH + CH_3$ products ($(1)^3A' + (1)^3A''$). As some ab initio calculations had shown that the shapes of the two PES are quite similar [3,12,14], we have assumed that they display the same reactivity. From Fig. 1a, it can be observed that the total cross-section for reaction (1) increases with E_T, as expected for a reaction with an energy barrier along the minimum energy reaction path (MEP) [31]. The increase of σ_r is due to both an increase in the reaction probability (0.7% at 0.50 eV and 11.6% at 2.0 eV for σ_r^{GHMS}) and the maximum reactive impact parameter, b_{max} (1.25 Å at 0.50 eV and 2.23 Å at 2.0 eV for σ_r^{GHMS}). Both properties show a similar behaviour than σ_r with E_T.

The ability of the vibrational energy of reactants to promote the reactivity of the $O(^3P) + CH_4$ system has also been analysed. To deal with this, the total reaction cross-sections of the process at $E_T = 0.65$ and 1.0 eV have been calculated considering the H–(CH_3) molecule to be in the $v = 0, 1$ and 2 levels. From these calculations it has been concluded that the traslational energy is more efficient than the vibrational energy in order to favour the reactivity. This fact cannot be directly inferred from the location of the transition state of the reaction, as it does not correspond to an early barrier ($(R_{OH})_{TS}/(R_{OH})_{eq} = 1.25$ and $(R_{H(CH_3)})_{TS}/(R_{H(CH_3)})_{eq} = 1.14$). Thus, $\sigma_r = 1.27$, 2.87 and 3.72 Å^2 for $E_T = 0.65$ eV and $v = 2$ ($E_{total} = 1.67$ eV), $E_T = 1.0$ eV and $v = 1$ ($E_{total} = 1.63$ eV), and $E_T = 1.5$ eV and $v = 0$ ($E_{total} = 1.74$ eV), respectively. It was even observed that increasing the vibrational energy of reactants could eventually diminish the reactivity. For instance, it was found that for $E_T = 1.0$ eV and $v = 0, 1$ and 2, $\sigma_r = 1.95$, 2.87 and 2.40 Å^2, respectively.

The opacity functions, $P(b)$ vs. b, for the three values of collision energy considered in more detail (0.65, 1.0 and 1.5 eV) are depicted in Fig. 1b. The shape of the opacity function for reaction (1) seems to have little dependence on E_T. In all cases, $P(b)$ peaks at small b values and monotonically decreases with increasing b. The maximum reactive impact parameter increases with E_T and $P(b)$ broadens as collision energy rises. This is the behaviour expected for a reaction that evolves through an energy barrier [31].

Regarding the OH product energetics, Table 1 collects the vibrational distributions and the average rotational levels for each one of the vibrational levels populated at $E_T = 0.65$, 1.0 and 1.5 eV. The $OH(v' = 0, 1)$ rotational distributions obtained at these collision energies are plotted in Fig. 1c,d. A relatively small OH vibrational excitation is found, as the population in $v' = 0$ ($v' = 1$) accounts for 76–92% (23–8%) of the total population, the population in $v' = 2$ being essentially negligible. However, when compared with the statistical situation, the calculated $P(v' = 1)/P(v' = 0)$ population ratio is greater than the prior one, this deviation increasing with E_T. On the

Table 1
Vibrational populations and average rotational levels for the OH product arising from reaction (1)

E_T (eV)	$P(v')$ and $\langle N'_{v'} \rangle$[a]		
	$v' = 0$	$v' = 1$	$v' = 2$
0.65	0.92 ± 0.02	0.08 ± 0.005	
	(3.8 ± 0.2)	(1.6 ± 0.4)	
1.00	0.84 ± 0.01	0.16 ± 0.005	0.0003 ± 0.002
	(6.1 ± 0.2)	(3.1 ± 0.2)	(1.5 ± 0.7)
1.50	0.76 ± 0.02	0.23 ± 0.006	0.005 ± 0.0008
	(8.5 ± 0.2)	(6.2 ± 0.3)	(3.2 ± 0.8)

[a] For each vibrational level and collision energy, the first given value corresponds to the vibrational population, while the second one appearing in parentheses is the average rotational level.

other hand, despite the fact that the vibrational distribution of the OH product becomes a little more excited as E_T increases, the fraction of available energy channeled into OH vibration diminishes with collision energy. Thus, the average fraction of available energy appearing as vibrational energy is $\langle f'_V \rangle = 0.44$, 0.30 and 0.22 for $E_T = 0.65$, 1.0 and 1.5 eV, respectively. This decrease is mainly accompanied by an increase of the available energy disposed as final translational energy ($\langle f'_T \rangle = 0.46$, 0.58 and 0.63, respectively).

Otherwise, a minor fraction of available energy is channeled into OH rotation, being $\langle f'_R \rangle = 0.10$, 0.12 and 0.15 for $E_T = 0.65$, 1.0 and 1.5 eV, respectively. A consequence of this slight increase in average rotational energy with E_T is that the $OH(v' = 0, 1)$ rotational distributions broaden and their population maxima shift towards higher values of N' as E_T increases. In fact, while the $OH(v' = 0, 1)$ rotational distributions are less excited than the statistical ones for $E_T = 0.65$ eV, they reproduce the statistical situation for $E_T = 1.0$ eV, and for $E_T = 1.5$ eV they clearly show the presence of an excited high-N' component that is not accounted for by the statistical distributions. This bimodal feature of the measured $OH(v' = 0, 1)$ rotational distributions is also observed for $E_T = 1.0$ eV, though it accentuates with increasing collision energy. This fact can be explained in terms of the microscopic reaction mechanism and will be discussed in Section 5.

3.2. Two-vector properties

The analysis of the angular momentum transformation from reactants to products was examined at all the energies used for the determination of the excitation function. An efficient conversion of orbital angular momentum ($\boldsymbol{J} \approx \boldsymbol{l} \rightarrow \boldsymbol{l}'$, with $\boldsymbol{J}$ being the total angular momentum vector) was observed in all the analysed cases, as expected for a reaction with a heavy–light–heavy (H–L–H) kinematics.

Fig. 2 collects the solid angle differential cross-sections ($d^2\sigma_r/d\omega'$), DCS hereafter, for the double vector correlations between initial ($\boldsymbol{k}$) and final ($\boldsymbol{k}'$) relative velocity vectors ($\boldsymbol{kk}'$), between $\boldsymbol{k}$ and final rotational angular momentum $\boldsymbol{j}'$ ($\boldsymbol{kj}'$), between $\boldsymbol{k}'$ and $\boldsymbol{j}'$ ($\boldsymbol{k}'\boldsymbol{j}'$) and between $\boldsymbol{l}'$ and $\boldsymbol{j}'$ ($\boldsymbol{l}'\boldsymbol{j}'$) for $E_T = 0.65$, 1.0 and 1.5 eV. The distributions are normalised to unit area to stress the similarities and differences among them at different collisional energies.

The $\boldsymbol{kk}'$ DCS depicted in Fig. 2a show a preference for backward scattering at all collision energies, although there is an increase in sideways and forward scattering as E_T rises. This trend is illustrated by the values of the average scattering angle ($\langle \theta_{\boldsymbol{kk}'} \rangle$) and the ratio of OH products recoiled in the forward ($\theta_{\boldsymbol{kk}'} < 90°$) and backward ($\theta_{\boldsymbol{kk}'} > 90°$) hemisphere ($f/b$ ratio). For $E_T = 0.65$, 1.0 and 1.5 eV, it has been obtained $\langle \theta_{\boldsymbol{kk}'} \rangle = 120.6°$, 107.2°, 95.1° and $f/b = 0.16$, 0.44, 0.90, respectively. This behaviour correlates with an increase in b_{max} as well as an increasing fraction of reactive trajectories at high initial impact parameters (see Fig. 1b) on rising E_T. Analysis of the dependence of the $\boldsymbol{kk}'$ distribution with impact parameter showed that the scattering in the forward hemisphere is only produced in reactive trajectories with high values of b. This result can be rationalised with the equation

$$\theta_{\boldsymbol{kk}'}(b, E_T) = \lambda(b)/E_T, \tag{2}$$

which has been derived for a direct reaction evolving through an energy barrier [31]. In Eq. (2) $\lambda(b)$ is a function of the impact parameter and $\theta_{\boldsymbol{kk}'}(b, E_T)$ is the scattering function that gives the scattering angle for fixed values of b and E_T. From this expression it comes out that for a given value of the impact parameter, more forward scattering must be expected as the collision energy increases. This is a consequence of the fact that the exploration of more repulsive regions of the PES as E_T rises cannot counterbalance the increasing impulsive effect, which favours the forward scattering.

The $\boldsymbol{l}'\boldsymbol{j}'$ DCS given in Fig. 2b are quite symmetrical and they show a substantial degree of alignment between both vectors at the three energies. A similar behaviour occurs for the $\boldsymbol{lj}'$ correlation.

The $\boldsymbol{kj}'$ and $\boldsymbol{k}'\boldsymbol{j}'$ DCS are collected in Fig. 2c,d and correspond to symmetrical distributions (as they must be) peaked at around 90°, just as it should be expected due to the above-mentioned tendency to dispose the $\boldsymbol{l}$ and $\boldsymbol{l}'$ vectors parallel or

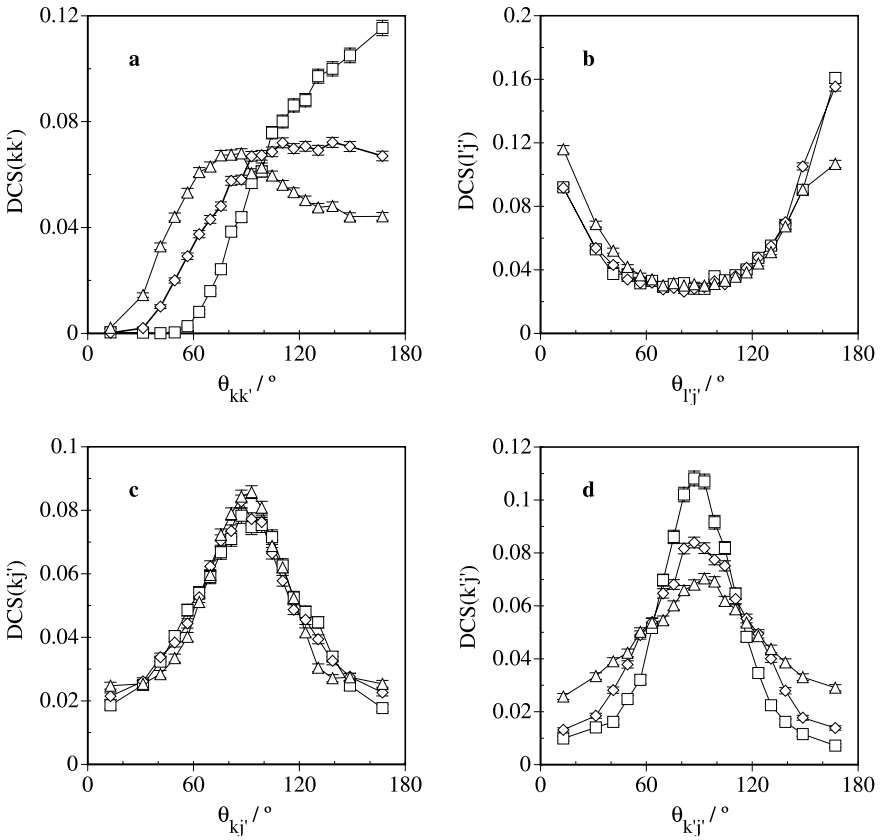

Fig. 2. (a) $\boldsymbol{kk'}$, (b) $\boldsymbol{l'j'}$, (c) $\boldsymbol{kj'}$ and (d) $\boldsymbol{k'j'}$ two-vector correlations expressed as solid angle differential cross-sections for $E_T = 0.65$ (□), 1.0 (◇) and 1.5 (△) eV. All DCS are normalised to unity.

antiparallel to $\boldsymbol{j'}$. In the case of the $\boldsymbol{k'j'}$ DCS an increasing contribution of the tails of the distribution is observed as E_T increases.

4. Product state-resolved reaction dynamics

To improve the understanding of the dynamics of the title reaction, we analysed the properties of products born in $v' = 0$ at some of three adjacent N' intervals, which roughly correspond to low-, intermediate- and high-N' values of the rotational distribution. The channels leading to products in $v' = 1$ and higher vibrational levels have a low yield (less than 0.25 in the most favourable case) and their product state-resolved properties will not be discussed.

Fig. 3 shows the unit area normalised product state-specific opacity functions at $E_T = 0.65$, 1.0 and 1.5 eV. At all collisional energies, $P(b)$ for low- and intermediate-N' have similar shapes, being broader and reaching higher b_{max} values than for high-N'. Thus, for high-N' values, 90% of the reactive trajectories are produced below 1.59 and 1.70 Å at $E_T = 1.0$ and 1.5 eV, respectively.

The product state-selected $\boldsymbol{kk'}$ DCS collected in Fig. 4a show that the formation of low- and intermediate-N' OH$(v' = 0)$ results in similar scattering distributions, whose backward feature strongly diminishes as E_T increases. Otherwise, for high-N' values more backward $\boldsymbol{kk'}$ distributions are obtained, though this behaviour is also softened with E_T. As a matter a fact, the $\boldsymbol{kk'}$ DCS evolves from backward to sideways with

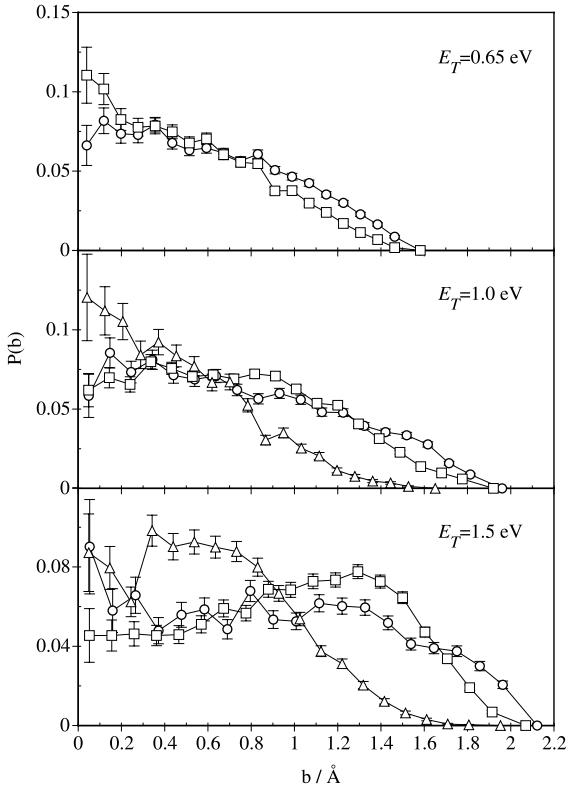

Fig. 3. OH($v' = 0$) product state-specific opacity functions. Low-N' (◯, $N' = 1$–4 for $E_T = 0.65$, 1.0 and 1.5 eV), medium-N' (□, $N' = 6$–9 for 0.65 eV, $N' = 7$–10 for 1.0 eV and $N' = 8$–11 for 1.5 eV) and high-N' (△, $N' = 13$–16 for 1.0 eV and $N' = 15$–18 for 1.5 eV) intervals have been considered. All $P(b)$ functions are normalised to unit area.

increasing E_T and decreasing N'. The f/b ratios are equal to 0.22, 0.5, 1.36 for low-N', 0.10, 0.48, 1.58 for medium-N' and 0.06, 0.49 for high-N' at $E_T = 0.65$, 1.0 and 1.5 eV. These trends are also observed in the average scattering angles for each of the aforementioned collision energies: $\langle\theta_{\boldsymbol{kk'}}\rangle =$ 120.6°, 104.6°, 87.0° for low-N', $\langle\theta_{\boldsymbol{kk'}}\rangle = 111.6°$, 105.0°, 85.0° for intermediate-N' and $\langle\theta_{\boldsymbol{kk'}}\rangle =$ 127.2°, 105.1° for high-N'.

The product state-selected $\boldsymbol{kj'}$ DCS correspond to symmetric distributions (as they must be) with a tendency of $\boldsymbol{j'}$ to lie perpendicular to $\boldsymbol{k}$. The strength of this correlation rises with increasing N', as can be observed in Fig. 4b. The state-selected DCS reveal that the tails of the distribution arise from the contributions of low-N' and medium-N' reactive trajectories. Given the relative population of each rovibrational level, overall DCS (see Fig. 2c) show no sensitivity to the collision energy. A similar behaviour is observed in what regards the product state-selected $\boldsymbol{k'j'}$ DCS, though in this case the broadening of the $\boldsymbol{k'j'}$ distributions on increasing E_T and decreasing N' is directly observed in the overall DCS (see Fig. 2d). The product state-selected $\boldsymbol{l'j'}$ DCS show a tendency of both vectors to lie parallel or antiparallel to each other. The distributions are sharper as N' increases and broaden with increasing collision energy, becoming almost isotropic for low N' at 1.50 eV.

5. Microscopic reaction mechanism

The microscopic mechanism of reaction (1) was studied in detail by analysing the temporal dependence of the interatomic distances, angles and potential energy of the system for samples of reactive trajectories obtained at different values of E_T. In all cases the evolution from reactants to products is due to a direct abstraction microscopic reaction mechanism.

A deeper insight into the reaction mode was obtained by analysing the geometries and energies of the system in the strong interaction region corresponding to different values of the distance between the attacking oxygen atom and the center of mass of the pseudodiatomic H–(CH_3) molecule, RSHELL [3]. The lowest RSHELL distance reached (min(RSHELL)) was determined for all the reactive trajectories at $E_T = 0.65$, 1.0 and 1.5 eV, which allowed us to obtain a rough idea about the properties of the 'turning point' of the reaction. Then, depending on the min(RSHELL) distances reached, all the reactive trajectories obtained were divided into two groups. Taking into account the features established for these two groups of reactive trajectories, which will be shown below, they were classified as rebound and non-rebound trajectories. For each collision energy considered, the reactive trajectories with lower values of min(RSHELL) were assigned to a rebound-type abstraction mechanism, and the remaining ones with higher values of min(RSHELL) were attributed to a non-rebound mechanism.

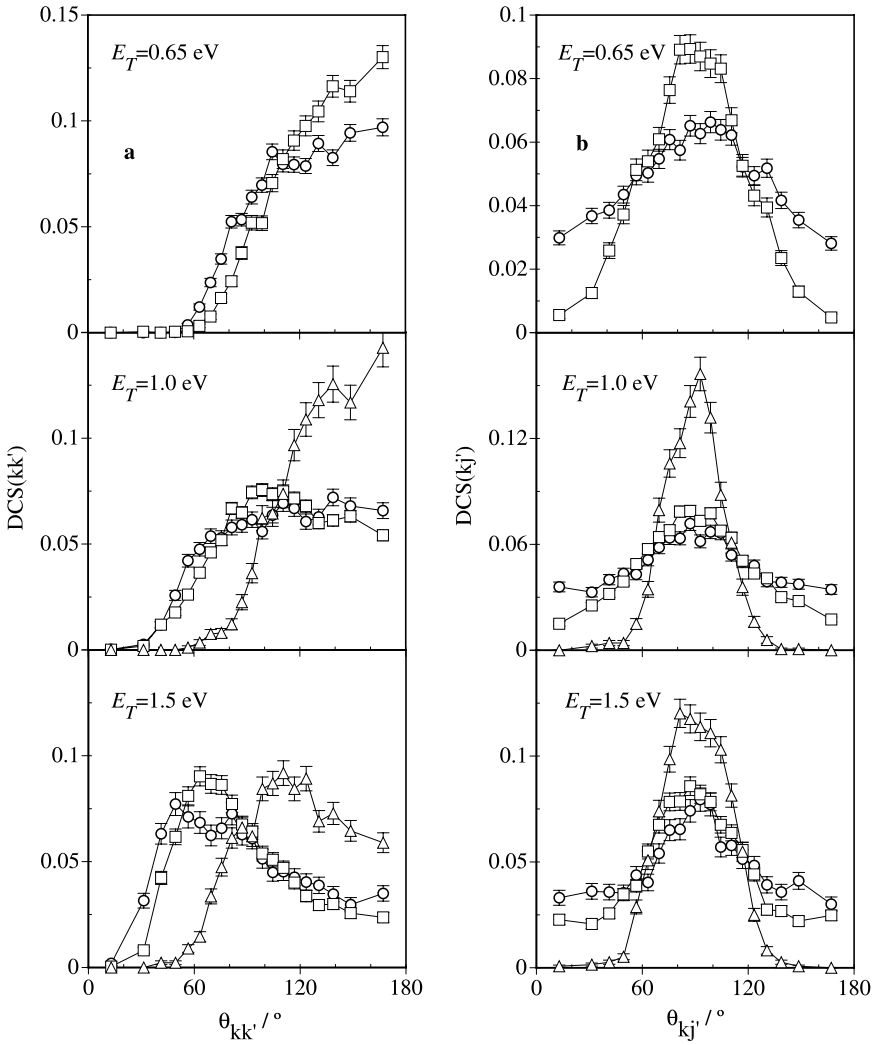

Fig. 4. OH($v' = 0$) product state-specific (a) $\boldsymbol{kk'}$ and (b) $\boldsymbol{kj'}$ two-vector correlations. Low-N' (◯, $N' = 1$–4 for $E_T = 0.65$, 1.0 and 1.5 eV), medium-N' (□, $N' = 6$–9 for 0.65 eV, $N' = 7$–10 for 1.0 eV and $N' = 8$–11 for 1.5 eV) and high-N' (△, $N' = 13$–16 for 1.0 eV and $N' = 15$–18 for 1.5 eV) intervals have been considered. All DCS are normalised to unity.

In Table 2 are given the contributions of the rebound and non-rebound reactive trajectories to reaction (1) at the three energies considered. As can be seen, the yield of the non-rebound mechanism is small at low values of E_T, but it increases as E_T rises. Also shown in Table 2 are the average geometries and potential energies of the 'turning points' determined for a sample of 100 reactive trajectories of the rebound and non-rebound types at the above-mentioned conditions of E_T. It was obtained that, as indicated in the min(RSHELL) calculation, the non-rebound trajectories present larger turning points'. Moreover, it was also observed that the non-rebound turning points' were closer to the geometry of the transition state of the PES, which is collinear, and corresponded to lower values of the potential energy. In fact, it was obtained that, in general, the rebound reactive trajectories explored more repulsive regions of the PES, as can be inferred from the average values shown in Table 2 of the maximum potential energy reached by the reactive trajectories. This behaviour

Table 2
Properties of the rebound and non-rebound reactive trajectories

E_T (eV)		Yield	Turning point'				$\langle E_{max}\rangle$[a] (eV)
			$\langle R_{OH}\rangle$ (Å)	$\langle R_{H(CH3)}\rangle$ (Å)	$\langle \angle OH(CH_3)\rangle$ (°)	$\langle E\rangle$ (eV)[a]	
0.65	Rebound	0.90	1.29 ± 0.02	1.22 ± 0.06	153.0 ± 12.4	0.66 ± 0.07	0.75 ± 0.05
	Non-rebound	0.10	1.28 ± 0.02	1.28 ± 0.02	163.9 ± 7.9	0.59 ± 0.03	0.66 ± 0.04
1.0	Rebound	0.55	1.29 ± 0.02	1.20 ± 0.07	137.4 ± 10.7	0.82 ± 0.12	1.02 ± 0.10
	Non-rebound	0.45	1.29 ± 0.02	1.22 ± 0.06	150.5 ± 12.9	0.68 ± 0.08	0.82 ± 0.10
1.5	Rebound	0.33	1.29 ± 0.01	1.18 ± 0.08	110.7 ± 15.8	1.07 ± 0.20	1.33 ± 0.19
	Non-rebound	0.67	1.28 ± 0.02	1.21 ± 0.06	136.6 ± 14.7	0.83 ± 0.16	1.00 ± 0.19

[a] Average potential energy at the 'turning point' ($\langle E\rangle$) and average maximum potential energy ($\langle E_{max}\rangle$) reached by the reactive trajectories referred to reactants.

is connected with the different type of dynamical properties established for the rebound and non-rebound mechanisms.

Fig. 5a collects the opacity functions corresponding to the rebound and non-rebound reactive trajectories at $E_T = 0.65$, 1.0 and 1.5 eV. For the rebound-type reactive trajectories, the maximum reaction probability arises for small values of b, then the reaction probability monotonically decreasing as b increases. For the non-rebound

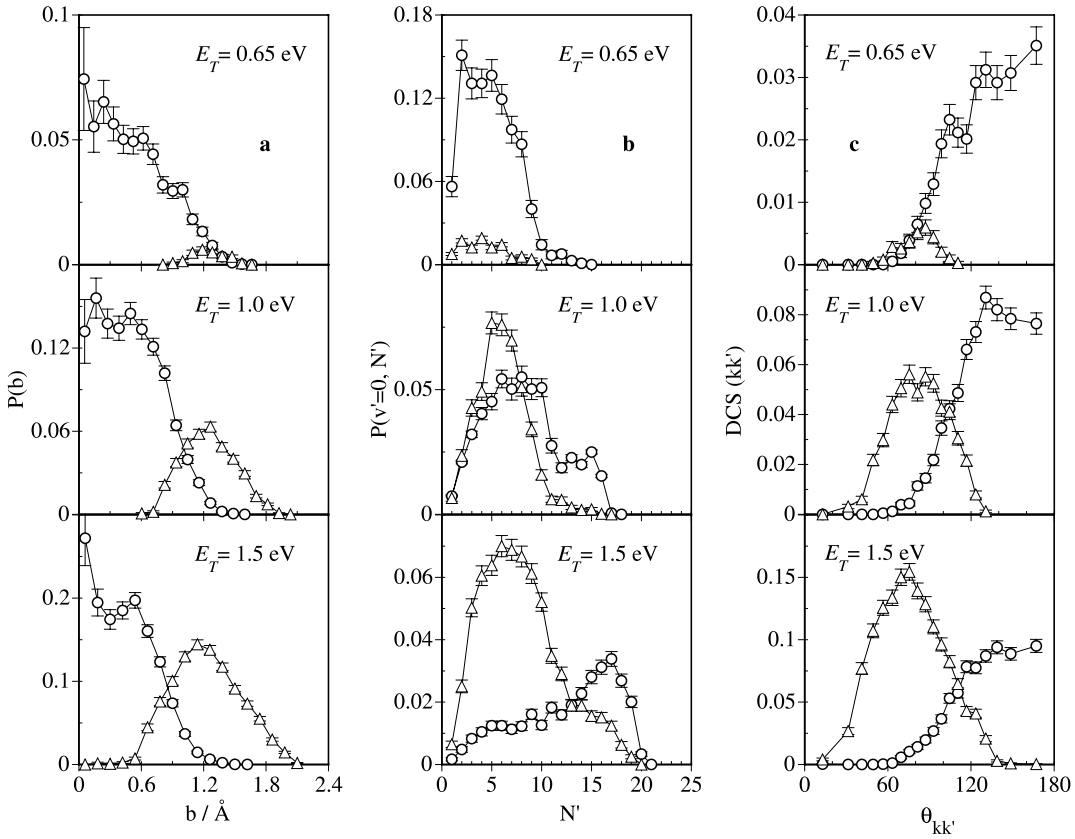

Fig. 5. (a) Opacity functions, (b) OH($v' = 0$) rotational distributions and (c) $\boldsymbol{kk'}$ DCS for rebound (◯) and non-rebound (△) trajectories at $E_T = 0.65$, 1.0 and 1.5 eV. The sum of the rotational populations for rebound and non-rebound is normalized to unity, and the DCS is given in $Å^2$ sr^{-1}.

reactive trajectories, the reactivity is strongly favoured for high values of the impact parameter.

The rotational distributions of $OH(v' = 0)$ arising from the rebound and non-rebound microscopic mechanisms at the three E_T values explored are shown in Fig. 5b. As E_T increases, significant differences appear in the rotational distributions corresponding to each mechanism, more rotational excitation being observed for the rebound-type reaction mode. This fact, which can be explained on the basis that rebound reactive trajectories explore more repulsive regions of the PES, accounts for the bimodal structure observed in the overall rotational distributions of the OH product (see Fig. 1c).

Fig. 5c shows the $\boldsymbol{kk'}$ DCS corresponding to the two different abstraction mechanisms considered. Clearly, the rebound-type reaction mode leads to backward distributions, while the non-rebound one furnishes sideways scattering, just as it must be expected since the former mechanism evolves through more repulsive regions of the PES. However, although more repulsive regions of the PES are explored when raising E_T for both reaction modes, then, not only is an increasing trend to forward scattering observed, but it is obtained that the backward feature of the rebound trajectories diminishes and the contribution of the sideways-type non-rebound trajectories increases. This fact might be due to the influence of the impulsive effect. Concerning other kinds of of two-vector properties, some differences also appear between both mechanisms regarding the $\boldsymbol{kj'}$ and $\boldsymbol{k'j'}$ correlations. The $\boldsymbol{kj'}$ DCS are broader in the case of the non-rebound mechanism, while the tendency for these two vectors to lie perpendicular is stronger for the rebound-type trajectories. The same behaviour was observed for the $\boldsymbol{k'j'}$ distribution. Finally, minor differences were obtained between both mechanisms concerning the $\boldsymbol{l'j'}$ correlation.

6. Summary and conclusions

A study of the collision energy effects on the dynamics of the reaction $O(^3P) + CH_4 \rightarrow OH + CH_3$ was performed using the QCT method and an analytical triatomic potential energy surface recently derived by our group. Scalar and two-vector properties of the reaction were analysed in terms of the collision energy, and also a product state-resolved study of the reaction dynamics was carried out. The features established are explained on the basis of the coexistence of two different types of abstraction reactive trajectories, rebound and non-rebound reactive trajectories, the contribution of the latter increasing with E_T. The rebound reactive trajectories are promoted by low impact parameters, lead to backward scattering and furnish more rotational excitation of the OH product, which is explained by the fact that more repulsive regions of the PES are explored. On the contrary, the non-rebound reactive trajectories are promoted by high impact parameters and lead to sideways scattering and lower OH rotational excitation than the rebound reaction mode. This work represents a starting point in the detailed study of the reaction dynamics of this prototypic polyatomic system. More rigorous studies including both the full dimensionality of the system and the possibility of quantum effects should be carried out in future.

Acknowledgements

This work was supported by the 'Dirección General de Enseñanza Superior' of the Spanish Ministry of Education and Culture through the DGES projects PB98-1209-C02-01 and -02. Financial support from the 'Generalitat de Catalunya' (Autonomous Government of Catalonia), ref. 2000SGR 00016, is also acknowledged. J.H. thanks the CIRIT from the Generalitat de Catalunya for a predoctoral research grant. The authors are also grateful to the 'Centre de Supercomputació i Comunicacions de Catalunya (C4-CESCA/CEPBA)' for the computer time made available.

References

[1] M.W. Chase Jr., C.A. Davies, J.R. Downey Jr., D.J. Frurip, R.A. McDonald, A.N. Syverud, J. Phys. Chem. Ref. Data 14 (Suppl. 1) (1985).

[2] J. Warnatz, in: W.C. Gardiner Jr., (Ed.), Combustion Chemistry, Springer, Berlin, 1984, p. 127.

[3] M. González, J. Hernando, J. Millán, R. Sayós, J. Chem. Phys. 110 (1999) 7326.
[4] J.W. Sutherland, J.V. Michael, R.B. Klemm, J. Phys. Chem. 90 (1986) 5941.
[5] N. Cohen, K.R. Westberg, J. Phys. Chem. Ref. Data 20 (1991) 1211.
[6] D.L. Baulch, C.J. Cobos, R.A. Cox, G. Hayman, T.h. Just, J.A. Kerr, T. Murrells, M.J. Pilling, J. Troe, R.W. Walker, J. Warnatz, J. Phys. Chem. Ref. Data 21 (1992) 445.
[7] A. Miyoshi, K. Ohmori, K. Tsuchiya, H. Matsui, Chem. Phys. Lett. 204 (1993) 241.
[8] A. Miyoshi, K. Tsuchiya, N. Yamauchi, H. Matsui, J. Phys. Chem. 98 (1994) 11452.
[9] T. Suzuki, E. Hirota, J. Chem. Phys. 98 (1993) 2387.
[10] G.M. Sweeney, A. Watson, K.G. McKendrick, J. Chem. Phys. 106 (1997) 9172.
[11] S.P. Walch, T.H. Dunning Jr., J. Chem. Phys. 72 (1980) 3221.
[12] C. González, J.J.W. McDouall, H.B. Schlegel, J. Phys. Chem. 94 (1990) 7467.
[13] B.S. Jursic, Int. J. Quantum Chem. 65 (1997) 75.
[14] J.C. Corchado, J. Espinosa-García, O. Roberto-Neto, Y.-Y. Chuang, D.G. Truhlar, J. Phys. Chem. A 102 (1998) 4899.
[15] O. Roberto-Neto, F.B.C. Machado, D.G. Truhlar, J. Chem. Phys. 111 (1999) 10046.
[16] J. Espinosa-García, J.C. García-Bernáldez, Phys. Chem. Chem. Phys. 2 (2000) 2345.
[17] D.C. Clary, Phys. Chem. Chem. Phys. 1 (1999) 1173.
[18] H.G. Yu, G. Nyman, J. Chem. Phys. 112 (2000) 238.
[19] J. Palma, D.C. Clary, J. Chem. Phys. 112 (2000) 1859.
[20] J. Palma, D.C. Clary, Phys. Chem. Chem. Phys. 2 (2000) 4105.
[21] G.M. Sweeney, K.G. McKendrick, J. Chem. Phys. 106 (1997) 9182.
[22] R.N. Porter, L.M. Raff, in: W.H. Miller (Ed.), Dynamics of Molecular Collisions Part B, Plenum, New York, 1976, p. 1.
[23] D.G. Truhlar, J.T. Muckerman, in: R.B. Bernstein (Ed.), Atom–Molecule Collision Theory: A Guide for the Experimentalist, Plenum, New York, 1979, p. 505.
[24] H.R. Mayne, Int. Rev. Phys. Chem. 10 (1991) 107.
[25] R. Sayós, M. González, TRIQCT (unpublished programme).
[26] M. González, D. Troya, M.P. Puyuelo, R. Sayós, P.A. Enríquez, Chem. Phys. Lett. 300 (1999) 603.
[27] M. González, J. Hernando, I. Baños, R. Sayós, J. Chem. Phys. 111 (1999) 8913.
[28] M. González, M.P. Puyuelo, J. Hernando, R. Sayós, P.A. Enríquez, J. Guallar, I. Baños, J. Phys. Chem. A 104 (2000) 521.
[29] M. González, J. Hernando, M.P. Puyuelo, R. Sayós, J. Chem. Phys. 113 (2000) 6748.
[30] R. Sayós, C. Oliva, M. González, J. Chem. Phys. 113 (2000) 6736.
[31] R.D. Levine, R.B. Bernstein, Molecular Reaction Dynamics, Oxford University Press, New York, 1987.